

# Geophysical Research Letters



## RESEARCH LETTER

10.1029/2020GL091378

### Key Points:

- Coastal Global Navigation Satellite Systems (GNSS) stations detect sea surface reflections that capture real-time sea level variations due to tides, tsunami waves, and storm surges
- Repeated tsunami surges of ~30 cm are observed around the Shumagin Islands for more than 10 h after the 2020 Shumagin earthquake
- A peak storm surge of ~2.5 m was observed as the eye of Hurricane Laura passed over a GNSS station on the Louisiana Coast

### Supporting Information:

- Supporting Information S1

### Correspondence to:

K. M. Larson,  
[kristinem.larson@gmail.com](mailto:kristinem.larson@gmail.com)

### Citation:

Larson, K. M., Lay, T., Yamazaki, Y., Cheung, K. F., Ye, L., Williams, S. D. P., & Davis, J. L. (2021). Dynamic sea level variation from GNSS: 2020 Shumagin earthquake tsunami resonance and Hurricane Laura. *Geophysical Research Letters*, 48, e2020GL091378. <https://doi.org/10.1029/2020GL091378>






Received 27 OCT 2020

Accepted 20 DEC 2020

© 2020. The Authors.

This is an open access article under the terms of the [Creative Commons Attribution-NonCommercial License](https://creativecommons.org/licenses/by-nc/4.0/), which permits use, distribution and reproduction in any medium, provided the original work is properly cited and is not used for commercial purposes.

## Dynamic Sea Level Variation From GNSS: 2020 Shumagin Earthquake Tsunami Resonance and Hurricane Laura

Kristine M. Larson<sup>1</sup> , Thorne Lay<sup>2</sup> , Yoshiki Yamazaki<sup>3</sup> , Kwok Fai Cheung<sup>3</sup> , Lingling Ye<sup>4</sup> , Simon D.P. Williams<sup>5</sup> , and James L. Davis<sup>6</sup> 

<sup>1</sup>Department of Aerospace Engineering Sciences, University of Colorado, Boulder, CO, USA, <sup>2</sup>Department of Earth and Planetary Sciences, University of California, Santa Cruz, CA, USA, <sup>3</sup>Department of Ocean and Resources Engineering, University of Hawaii at Manoa, Honolulu, HI, USA, <sup>4</sup>School of Earth Sciences and Engineering, Guangdong Provincial Key Lab of Geodynamics and Geohazards, Sun Yat-sen University, Guangzhou, China, <sup>5</sup>Marine Physics and Ocean Climate Group, National Oceanography Centre, Liverpool, UK, <sup>6</sup>Division of Seismology, Geology, and Tectonophysics, Lamont Doherty Earth Observatory, Columbia University, Palisades, NY, USA

**Abstract** Rapid determination of sea level variations caused by tsunamis or major storm surges is important for coastal hazard mitigation. Coastal Global Navigation Satellite Systems (GNSS) stations at elevations less than ~300 m can record time-varying sea level changes by tracking signals that reflect from the sea surface, relative to direct signals from the satellites. We demonstrate that such GNSS stations can rapidly provide local sea level measurements for a near-field tsunami, involving many hours of shelf resonance generated by the 2020 Shumagin earthquake as well as for the storm surge accompanying passage of the eye of Hurricane Laura over the Louisiana Coast. Coastal GNSS stations deployed to measure tectonic deformation and co-seismic displacements can inexpensively augment the spatial sampling provided by tide gauges for measuring tsunami-induced coastal resonance and storm surges. This information can guide response activities during the crucial initial hours of an event.

**Plain Language Summary** Sea level variations caused by tsunamis and storm surges must be measured as quickly as possible for public safety warnings. This work uses examples from the 2020 Shumagin Island tsunami and the Hurricane Laura storm surge to demonstrate that Global Navigation Satellite System instruments installed along coastal regions to measure plate tectonic motions are also capable of providing sea level information in near real-time.

## 1. Introduction

Tsunamis generated by offshore earthquakes, submarine slumps or volcanic eruptions, and storm surges generated by hurricanes have been responsible for great loss of life and destruction through time. Notable recent catastrophic tsunamis generated by the 2004 Sumatra-Andaman (e.g., Lay et al., 2005), 2010 Maule, Chile (e.g., Yoshimoto et al., 2016), and 2011 Tohoku, Japan (e.g., Yamazaki et al., 2018) earthquakes have caused vast damage over the last two decades. The first tsunami surge is often not the most devastating, due to both wave dispersion and generation of shelf resonance and edge waves (e.g., Geist, 2012) that can result in repeated surges with peak tsunami run-up occurring hours after the causative earthquake both in the near field (Melgar & Ruiz-Angulo, 2018; Yamazaki & Cheung, 2011) and far field (Cheung et al., 2013).

The dynamics of tsunami wave interactions along coastlines can be accurately modeled given detailed bathymetry, but each event has distinct properties that affect the subsequent impacts. Coastal tide-gauge observations tend to be sparse in many regions and are often located in harbors that generate complex local effects. As a result, decision-making regarding return of coastal residents and activities after passage of the first tsunami wave is often poorly informed regarding strength of any shelf resonance or edge waves that have been generated (e.g., Soulé, 2014).

Similarly, strong storm surges, particularly those associated with passage of a hurricane onto land, generate coastal flooding that can take a huge toll, as for events like 2005 Katrina (e.g., Fritz et al., 2007), 2012 Sandy (e.g., Chen et al., 2014), and 2013 Haiyan (e.g., Soria et al., 2006). The storm surge is a complex function of storm central pressure, wind intensity, storm forward speed as well as approach direction relative to the coast, width and slope of the ocean bottom, and local features and barriers, which also make precise

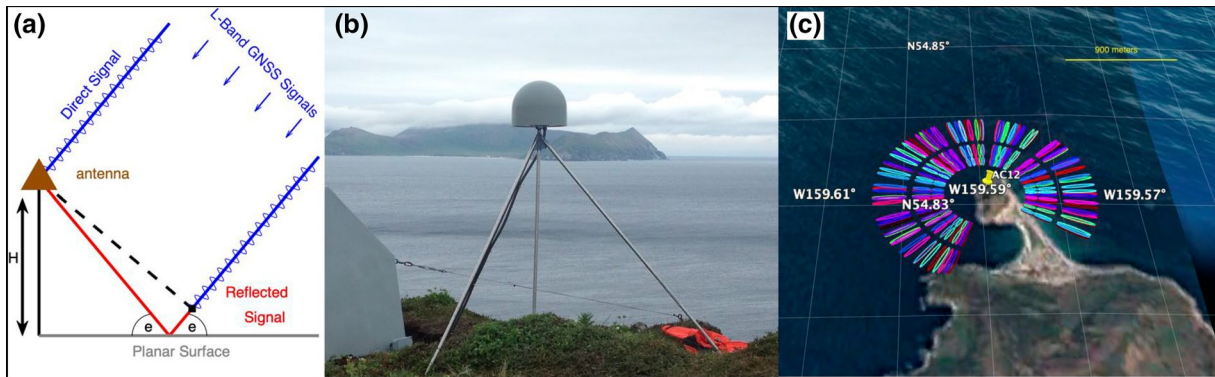


**Figure 1.** (a) Representation of reflected GNSS signal geometry.  $H$  is the vertical distance between the phase center of the GNSS antenna and the reflecting surface and  $e$  is the angle between the satellite and the horizon. Direct GNSS signals are shown in blue; the additional path traveled by the reflected signal is shown in red. (b) GNSS receiver AC12 on Chernabura Island, Alaska (Photo credit: UNAVCO). (c) Reflection zones shown in color were used for AC12 water level measurements (Roesler & Larson, 2018). Map courtesy of Google Earth.

advance prediction very challenging (e.g., <https://www.nhc.noaa.gov/surge/>). Both tsunamis and storm surges could be better quantified and predicted with more extensive real-time measurements of near-shore sea level variations.

Global Navigation Satellite Systems (GNSS) networks can provide these coastal sea level measurements. While traditionally these networks only tracked GPS signals at low sample rates (30 s) and were downloaded once per day, increasingly, the equipment is being upgraded to track the signals from up to four constellations with real-time streaming at high-rates. The high-rate three-dimensional positions derived from these GNSS data are already being used in earthquake and tsunami early warning applications (e.g., Melgar et al., 2016). Here we demonstrate that these same GNSS instruments can also play a key role in coastal hazard mitigation, by providing near-real-time assessments of sea level variation during tsunamis and storm surges. We use GNSS data collected during the recent Shumagin Islands earthquake/tsunami (July 22, 2020) and Hurricane Laura (landfall on August 27, 2020) to demonstrate both current capabilities and how these new applications can be improved by tracking signals from all four GNSS constellations.

## 2. Method: GNSS Interferometric Reflectometry

GNSS interferometric reflectometry (GNSS-IR) treats the GNSS system as a bistatic radar. The interference pattern created by the direct GNSS signal and a reflected signal from a planar surface below a GNSS antenna has a distinctive frequency that is related to  $H$ , the vertical distance between the antenna phase center and the reflecting surface (Figure 1a). The interference pattern is best observed using GNSS satellites at low elevation angles ( $e$ ). Generally, a single  $H$  value is estimated for each rising and setting satellite arc, thus, providing a sporadic time series of sea level values throughout the day. To use the method optimally, one must identify which GNSS satellite arcs reflect off water. The GNSS-IR method fails if the reflecting surface is very rough, as it would be expected during very high winds.

Each estimate of  $H$  is derived from the dominant frequency in the GNSS Signal-to-Noise Ratio (SNR) data. We derive the dominant SNR frequency ( $2H / \lambda$ , where  $\lambda$  is the GNSS wavelength) using a standard periodogram (Lomb Scargle Periodogram (LSP)) (Larson, 2020). Mapping software was used to choose the appropriate station azimuth and elevation angle mask shown in Figure 1c (Roesler and Larson, 2018). For the case where  $H$  is significantly changing during a satellite arc, an additional correction is required,  $2\dot{H} \tan e / \dot{e}$  (Larson et al. 2013b). Because this correction depends on  $\dot{e}$ , rising and setting GNSS satellite arcs will have corrections of different sign. For tidal studies, the  $\dot{H}$  term can be estimated simultaneously with the tidal parameters (Williams, 2020). For sites with relatively low values of  $H$  within an arc, improved precision can be achieved with retrieval methods that explicitly model the temporal variations within the satellite arc (Strandberg et al., 2016). However, these methods also make assumptions about the smoothness of those temporal variations that we do not consider here.

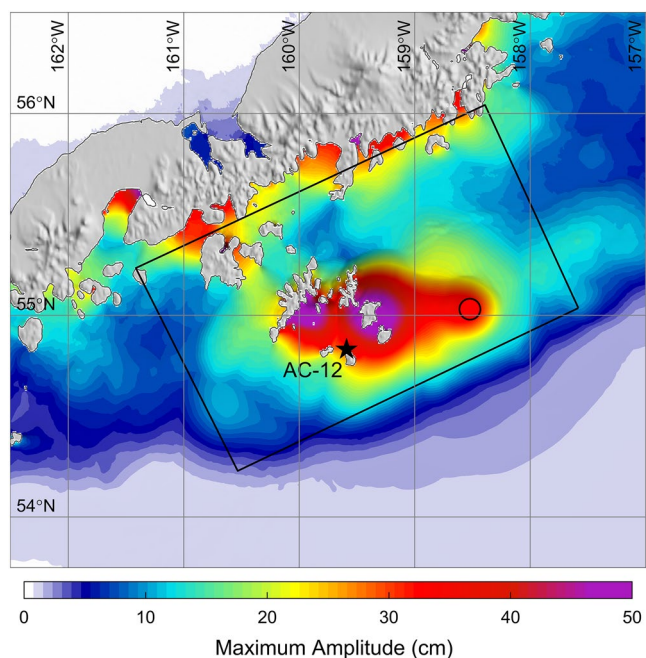


**Figure 2.** Maximum computed tsunami amplitude in the source region of the 2020 Shumagin Islands earthquake. The fault slip model (Figure S1) is delineated by the black rectangle and the epicenter of the earthquake is indicated by the circle. The location of GNSS station AC12 on Chernabura Island is indicated with the star. The large (>25 cm) sea-surface uplift area corresponds well with the slip distribution on the fault. The large tsunami amplitudes along the Alaskan Peninsula correspond to embayment oscillations coupled with standing edge waves over the continental shelf.

for the slip distribution based on global seismic body waves and regional GNSS displacements with fault placements guided by the Slab2 model (Hayes et al., 2018; Figure S1) is used to compute the time-varying sea level generated by the seafloor deformation. The tsunami calculation involved the nonhydrostatic model NEOWAVE with multilevel grid nesting for tsunami generation, propagation, and run-up (Yamazaki et al., 2009; 2011). A high-resolution bathymetry model (NCEI) around the Shumagin Islands embedded in a surrounding GEBCO model was used. Figure 2 displays the maximum computed sea-surface amplitude from the tsunami model in the vicinity of the Shumagin Islands. A very similar tsunami model is obtained using the slip inversion of Liu et al. (2020), with the configuration of the Shumagin Islands producing strong resonance within the ring of islands that is locally nonsensitive to details of the slip distribution. The tsunami generated by the earthquake had a maximum sea surface amplitude of ~50 cm, as expected for the moderate slip (<3.8 m) and depth of the faulting (20–45 km deep), but it was well-recorded by deep-water ocean bottom pressure sensors of the Deep-Ocean Assessment and Reporting of Tsunamis (DART) network operated by NOAA (DART, 2020). The recorded tsunami waves at the DART stations are less than 1 cm high, partly due to reverse shoaling of the waves as they crossed from the shallow continental shelf beneath which the rupture occurred into the deep Pacific Ocean.

GNSS-IR measurements of sea surface elevation at a telemetered GNSS station (AC12) (Figure 1b; Blewitt et al. 2018) above a large-slip region in the Shumagin earthquake are compared with model predictions. The tsunami model for our finite-fault inversion provides the time-varying sea level around the northern shore of Chernabura Island, where AC12 is located (Figure 2).

Thirty-one days of GPS data (June 28, 2020 to July 29, 2020) for station AC12 (<https://doi.org/10.7283/T5NV9G7P>) were analyzed to validate the azimuth and elevation angle mask (Figure 1c) and to estimate a background tidal model. The tidal signature is clearly visible in the initial  $H$  values (Figure S2). On an average, 93 estimates of  $H$  can be made per day at this site, but only 52 of these are at distinct times (i.e. 52 are L1

A GNSS-IR based tide gauge is the only tide measurement system that can simultaneously record the three-dimensional position of the antenna, meaning it can measure sea level in an absolute terrestrial reference frame. The accuracy of GNSS-IR as a tide gauge has been validated from subdaily (Larson et al. 2013a) to decadal time scales (Larson et al., 2017), but it has not previously been used to detect a tsunami or a major hurricane landfall.

### 3. Data

#### 3.1. Shumagin Earthquake

The Shumagin Islands earthquake on July 22, 2020 (06:12:44 UTC, 55.072°N, 158.596°W, 28 km deep,  $M_w = 7.8$ , USGS-NEIC: <https://earthquake.usgs.gov/earthquakes/eventpage/us7000asvb/executive>) involved underthrusting of the Pacific plate beneath the North American plate offshore of the Alaska Peninsula. The event has garnered great geophysical interest, due to its location within a portion of the plate boundary, previously identified as a seismic gap with high potential for hosting an earthquake with  $M_w$  8.2 or possibly much larger (Davies et al. 1981). In response to this concern, geodetic measurements, including high-rate GNSS observations, have been made on the Shumagin Islands for 35 years to quantify crustal strain accumulation. Current assessments suggest that much of the motion (60%–90%) between the plates along the Shumagin Gap is accommodated aseismically (e.g., Li & Freymueller, 2018).

The same GNSS stations, along with regional strong-motion and broadband seismic stations and the global seismic network, recorded the ground motions produced by the 2020 earthquake, and these data have been used to invert for time-varying slip distributions on the fault (e.g. USGS-NEIC; Crowell & Melgar, 2020; Liu et al., 2020). Our own inversion

retrievals and 41 are L2C). Each periodogram retrieval corresponds to a time period, defined by the satellite azimuth and the elevation angle range (Larson, 2020). At AC12, the time periods range from 10 to 28 min, with a median value of 14 min. A final  $H$  series was computed by removing (1) the vertical coseismic offset ( $\sim 0.33$  m, Figure S3) and (2) estimated tidal terms/tidal surface rates (Larson et al., 2017). The standard deviation of the  $H$  tidal fit is 0.121 m for this 30-day period (excluding the day of the earthquake). The residuals of  $H$  to the tidal fit (with the sign reversed) give us the water level measurements used in this study.

### 3.2. Hurricane Laura

$H$  was estimated for the Calcasieu Pass, Louisiana (CALC) GNSS data for the period between August 16, 2020 and September 13, 2020. The elevation and azimuth mask shown in Figure S4 was used.  $\dot{H}$  effects were removed using a tidal fit (Larson et al., 2017; Williams, 2020). The Calcasieu Pass receiver tracked signals from GPS, Galileo, and Glonass. A high number of 172 individual water level retrievals were made in a single day. The lowest number, 136, was retrieved on the day of the hurricane landfall (August 27, 2020).

We use the collocated NOAA tide gauge record as an accurate water level reference and calculate the standard deviations of the tide gauge- $H$  residuals. Water level precision at this site is significantly better than reported for AC12: 0.063–0.080 m, depending on the GNSS frequency. Larger elevation angle ranges could be used at CALC because it is located directly above the water; similar elevation angles at AC12 would have been reflecting off the island.

## 4. Results

Figure 3a shows GNSS-IR water level measurements (with tidal effects removed) and predicted water level for the earthquake-generated tsunami that would be observed at the AC12/Chernabura site. These GNSS-IR measurements depict differential motion of the sea surface relative to the uplifted land over the time period of each measurement ( $\sim 14$  min). As the GNSS-IR correction for the sea surface rate of change is positive or negative depending on whether the satellite is rising or setting in the sky, we colored-code the water level estimates accordingly.

We emphasize two boxed regions (I and II in Figure 3a) that show particularly discordant estimates (nearly a meter) between individual GNSS-IR estimates and the tsunami model sea level predictions. This discrepancy is eliminated when a sea surface elevation rate correction is applied to minimize the difference between time-coincident rising and setting satellite arcs (Figure 3b). This demonstrates the difficulty of using GNSS-IR at AC12 as an independent tsunami measurement system due to the relatively small number of such overlapping rising/setting satellite intervals. The AC12 GNSS site has not been upgraded since its installation in 2008 and thus only tracks GPS satellites. For time periods when no coincident rising/setting arcs are available, the sea level estimates in Figure 3b have been corrected using the tsunami model predicted surface velocities (these would not be available in real-time). The comparison in Figure 3c shows that the inferred sea surface velocities used for GNSS-IR for pairs of rising and setting observations are consistent with the tsunami model predictions for at least five cycles of sea level oscillations following the earthquake. We further see that the satellite observations without coincident rising/setting arcs are also consistent with the tsunami model predictions. The consistency provides mutual validation for both the GNSS-IR procedure and the tsunami calculation. The latter is based on an inverted slip distribution with uncertainty, an imperfect bathymetric model, and a complex nonhydrostatic tsunami calculation, so it is not directly observed sea level history, as would be provided by a tide gauge.

The sea level variation in Figure 3b is the computed dynamic response of the ocean layer from coseismic (0 h) 33 cm uplift of the land and surrounding seafloor, followed by the radiation of tsunami waves away from the region of uplift, then repeated surge and drawdown of the ocean with  $\sim 110$  min period due to trapping in the ring-like formation of the Shumagin Islands. The tsunami energy is also trapped by the shallow shelves along the Alaska Peninsula to establish  $\sim 90$  min period standing edge waves (Figure 2). Interference between the two harmonics produces a beat with a period of  $\sim 8$  h that is well captured by the corrected measurements. Given that the main slip patch on the fault extended beneath the Shumagin Islands, the signals in Figure 3b are directly from the initial tsunami excitation that radiates from the earth-

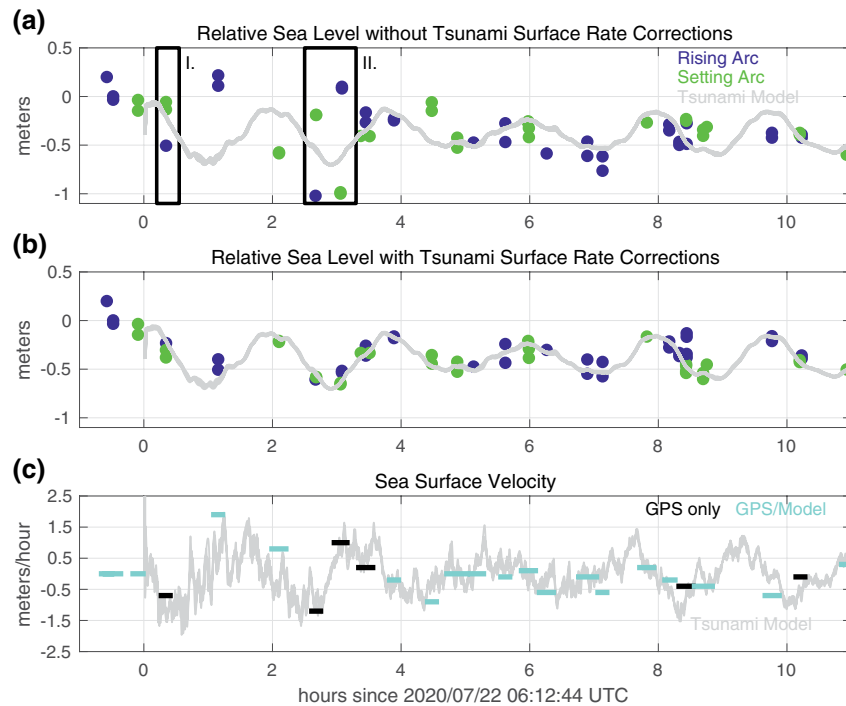


**Figure 3.** Sea level variation at GNSS station AC12 on Chernabura for GNSS-IR and the tsunami model. (a) Sea level estimates based on de-tided GNSS-IR relative sea level measurements for rising (blue) and setting (green) satellites and the tsunami model (gray). (b) Sea level measurements with corrections for sea surface velocity estimated from coincident rising (blue) and setting (green) observations or from the tsunami model (gray) for isolated observations. (c) Sea surface velocity from the tsunami model (gray), intervals for which the model velocity is used in b (cyan), and intervals for which the velocity is independently estimated from coincident rising and setting GNSS-IR observations (black). The line segment conveys the time interval for each satellite arc.

quake deformation zone. This is clearly an exceptional observation, but similar sea level measurements could be made from other coastal GNSS stations to capture direct tsunami and edge waves from more distant positions.

The observations in Figure 3b provide a time-history of the tsunami waves comparable to what is provided by a tide gauge, although the latter is commonly impacted by local harbor geometry. The tsunami generated by the 2020 Shumagin earthquake was modest in peak amplitude, and larger tsunami signals will produce even more robust observations. With multiple high-rate GNSS stations with telemetry along a coast, one can monitor the direct and resonating tsunami arrivals and edge waves over the entire region, providing a strong basis for decision-making about issuing all-clear messages to coastal populations and ships entering or leaving ports and harbors. The GNSS-IR measurements can also provide confidence in numerical and forecast models for coastal tsunami and edge wave time histories and amplitudes just as in Figure 3b.

How can we improve the tsunami monitoring capability of instruments at AC12 and other sites located in seismically active regions? The easiest solution is to replace GPS-only instruments with full GNSS-tracking units to increase the number of coincident rising and setting observations. Figure 4 summarizes, how frequently the Chernabura site would have been able to unambiguously measure tsunami waves on the day of the earthquake for the actual case of GPS-only versus the full GNSS constellation. The GPS unit can retrieve water level 32.6% of the time, while a GNSS unit retrieves sea level 90.3% of the time. Here we used the specific site mask (which limits the azimuthal directions to those facing the ocean) from Chernabura (Figure 1c), but clearly a GNSS instrument would greatly improve temporal resolution over a GPS-only instrument at any suitably located coastal station. This leads to a recommendation that geodesists and surveyors installing new GNSS sites, examine the potential for utilizing GNSS water reflections. In some locations, particularly where the terrain is very flat, moving a site only a few meters closer to the water makes the

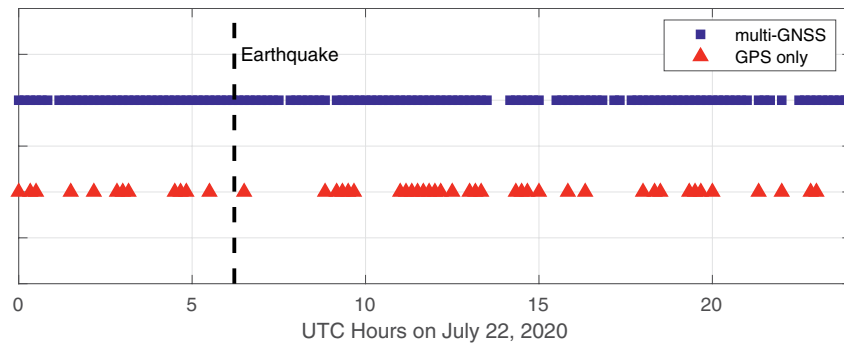


**Figure 4.** Time intervals of coincident satellite rising and setting arcs in view at Chernabura/AC12 calculated for ten-minute periods for GPS-only units and full GNSS-tracking units.

difference between a useable and nonuseable GNSS-IR site, with negligible impact on the precise positioning application.

In addition to providing real-time quantification of coastal tsunami signals, GNSS-IR can also provide critically important observations of storm surges (Peng et al., 2019). Hurricane Laura, which struck the Gulf Coast of the United States in late August 2020, provides a dramatic example, where a GNSS unit not only withstood 40 m/s winds without data loss, but GNSS-IR was able to accurately track the storm surge throughout the landfall of the event. Unlike Chernabura, where it is not possible to directly test GNSS-IR accuracy, the GNSS instrument at Calcasieu Pass, Louisiana, is collocated with a tide gauge and wind speed sensor operated by NOAA.

Figure 5a shows water level measurements made before, during, and after Hurricane Laura landfall using GPS, Russian (Glonass), and European (Galileo) satellites. The GNSS-IR measurements of water level agree well with the tide gauge. The GNSS-IR determinations can be reliably retrieved up to the point at

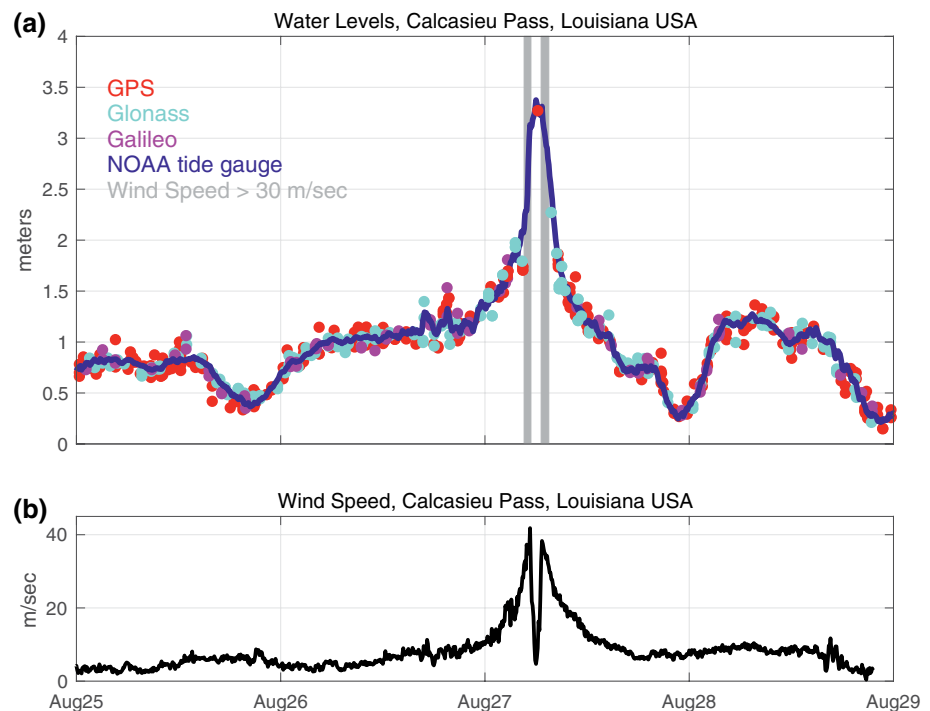


**Figure 5.** (a) Water levels measured at Calcasieu Pass, Louisiana, USA, with an acoustic tide gauge (NOAA) and GNSS-IR (this study) using GPS, Russian Glonass, and European Galileo satellites during Hurricane Laura. (b) Wind speed at the same location.

which sea-surface roughness prevents coherent specular reflection; in this study that point is shown to be wind speeds of  $\sim 30$  m/sec. As the eye of the hurricane passed directly over the site, a GNSS satellite signal happened to be at a grazing angle. As this coincided with a significant decrease in wind speed (Figure 5b) and correspondingly reduced water surface roughness, GNSS-IR was able to observe the peak storm surge detected by the tide gauge.

## 5. Conclusions

The 2020 Shumagin Islands earthquake involved substantial slip of several meters on the plate boundary directly below a GNSS sensor on Chernabura Island. Analysis of the GNSS sea surface reflections allows the estimation of dynamic sea-level variation, which is to be made in near real-time. Given that the station was near the peak uplift above the faulting, the GNSS sensor was essentially in the bullseye of tsunamigenic uplift, so relative draw-down of the ocean as the tsunami wave radiates from the source region can be directly observed by GNSS interferometric reflectometry. In this case, the ring-like formation of the Shumagin Islands established a 110 min resonance of sea level, with at least 10 h of ocean oscillations. This motivates deployment of multiconstellation GNSS capable receivers, adjacent to regions that may be exposed to large tsunamis from local or remote source regions, as a means of providing densified (relative to current tide gauge distributions) observation of propagating and standing edge waves in real time to assist in tsunami-warning and evacuation decision-making. The same GNSS observations can also provide valuable information about storm surges in coastal environments.

## Data Availability Statement

The high-resolution digital elevation model, Sand Point V2, at the Shumagin Islands was downloaded from the National Centers for Environmental Information (<https://maps.ngdc.noaa.gov/viewers/bathymetry/>). GNSS Data for AC12-ChernaburaAK2008 are available via <https://doi.org/10.7283/T5NV9G7P>. GNSS data for Calcasieu Pass (CALC) are available from the National Geodetic Survey: <https://www.ngs.noaa.gov/CORS/Sites/calc.html>. The NOAA tide gauge data are available from <https://tidesandcurrents.noaa.gov/stationhome.html?id=8768094>.

## Acknowledgments

The authors thank two anonymous reviewers for helping us improve the manuscript. NASA: Kristine Larson 80NSSC20K1731; NSF: Thorne Lay EAR1802364; NOAA: Yoshiki Yamazaki, Kwok Fai Cheung NA19N-WS4670012; National Natural Science Foundation of China (NSFC): Lingling Ye 41874056; Fundamental Research Funds for the Central Universities, Sun Yat-sen University: Lingling Ye 19lgzd11.

## References

- Blewitt, G., Hammond, W. C., & Kreemer, C. (2018). Harnessing the GPS data explosion for interdisciplinary sciences. *EOS*, 99. <https://doi.org/10.1029/2018EO104623>
- Chen, N., Han, G., Yang, J., & Chen, D. (2014). Hurricane Sandy storm surges observed by HY-2A satellite altimetry and tide gauges. *Journal of Geophysical Research: Oceans*, 119(7), 4542–4548. <https://doi.org/10.1002/2013JC009782>
- Cheung, K. F., Bai, Y., & Yamazaki, Y. (2013). Surges around the Hawaiian Islands from the 2011 Tohoku tsunami. *Journal of Geophysical Research: Oceans*, 118, 5703–5719. <https://doi.org/10.1002/jgrc.20413>
- Crowell, B. W., & Melgar, D. (2020). Slipping the Shumagin Gap: A kinematic coseismic and early afterslip model of the  $M_w$  7.8 Simeon Island, Alaska, earthquake. *Geophysical Research Letters*, 47(19), e2020GL090308. <https://doi.org/10.1029/2020GL090308>
- DART. (2020). <https://nctr.pmel.noaa.gov/Dart/>
- Davies, J., Sykes, L., House, L., & Jacob, K. (1981). Shumagin seismic gap, Alaskan Peninsula: History of great earthquakes, tectonic setting, and evidence for high seismic potential. *Journal of Geophysical Research*, 86, 3821–3855. <https://doi.org/10.1029/JB086iB05p03821>
- Fritz, H. M., Blount, C., Sokolowski, R., Singleton, J., Fuggle, A., McAdoo, B. G., et al. (2007). Hurricane Katrina storm surge distribution and field observations on the Mississippi Barrier Islands. *Estuarine, Coastal and Shelf Science*, 74, 12–20. <https://doi.org/10.1016/j.ecss.2007.03.015>
- Geist, E. L. (2012). Near-field tsunami edge waves and complex earthquake rupture. *Pure and Applied Geophysics*, 170(9–10), 1475–1491. <https://doi.org/10.1007/s00024-012-0491-7>
- Hayes, G. P., Moore, G. L., Portner, D. E., Hearne, M., Flamme, H., Furtney, M., & Smoczyk, G. M. (2018). Slab2, a comprehensive subduction zone geometry model. *Science*, 362(6410), 58–61. <https://doi.org/10.1126/science.aat4723>
- Larson, K. M. (2020). *GNSSREFL*. <https://pypi.org/project/gnssrefl/>
- Larson, K. M., Lofgren, J. S., & Haas, R. (2013a). Coastal sea level measurements using a single geodetic GPS receiver. *Advances in Space Research*, 51(8), 1301–1310. <https://doi.org/10.1016/j.asr.2012.04.017>
- Larson, K. M., Ray, R. D., Nievinski, F. G., & Freymueller, J. T. (2013b). The Accidental Tide Gauge: A GPS Reflections Case Study from Kachemak Bay, Alaska. *IEEE Geoscience and Remote Sensing Letters*, 10(5), 1200–1204. <https://doi.org/10.1109/LGRS.2012.2236075>
- Larson, K. M., Ray, R. D., & Williams, S. P. D. (2017). A ten-year comparison of water levels measured with a geodetic GPS receiver versus a conventional tide gauge. *Journal of Atmospheric and Oceanic Technology*, 34(2), 295–307. <https://doi.org/10.1002/2017JGL076761>
- Lay, T., Kanamori, H., Ammon, C. J., Nettles, M., Ward, S. N., Aster, R. C., et al. (2005). The great Sumatra-Andaman earthquake of 26 December 2004. *Science*, 308, 1127–1133. <https://doi.org/10.1126/science.1112250>

- Li, S., & Freymueller, J. T. (2018). Spatial variation of slip behavior beneath the Alaska Peninsula along Alaska-Aleutian subduction zone. *Geophysical Research Letters*, *45*, 3453–3460. <https://doi.org/10.1002/2017GL076761>
- Liu, C., Lay, T., Xiong, X., & Wen, Y. (2020). Rupture of the 2020  $M_w$  7.8 earthquake in the Shumagin gap inferred from seismic and geodetic observations. *Geophysical Research Letters*, *47*, e2020GL090806. <https://doi.org/10.1029/2020GL090806>
- Melgar, D., Allen, R. M., Riquelme, S., Geng, J., Bravo, F., Baez, J. C., et al. (2016). Local tsunami warnings: Perspectives from recent large events. *Geophysical Research Letters*, *43*, 1109–1117. <https://doi.org/10.1002/2015GL067100>
- Melgar, D., & Ruiz-Angulo, A. (2018). Long-lived tsunami edge waves and shelf resonance from the M8.2 Tehuantepec earthquake. *Geophysical Research Letters*, *45*, 12414–12421. <https://doi.org/10.1029/2018GL080823>
- Peng, D., Hill, E. M., Li, L., Switzer, A. D., & Larson, K. M. (2019). Applications of GNSS interferometric reflectometry for detecting storm surges. *GPS Solutions*, *23*, 47. <https://doi.org/10.1007/s10291-019-0838-y>
- Roesler, C. J., & Larson, K. M. (2018). Software Tools for GNSS Interferometric Reflectometry. *GPS Solutions*, *22*, 80. <https://doi.org/10.1007/s10291-018-0744-8>
- Soria, J. L. A., Switzer, A. D., Villanoy, C. L., Fritz, H. M., Bilgera, P. H. T., Cabrera, O. C., et al. (2006). Repeat storm surge disasters of Typhoon Haiyan and its 1897 predecessor in the Philippines. *Bulletin of the American Meteorological Society*, *97*(1), 31–48. <https://doi.org/10.1175/BAMS-D-14-00245.1>
- Soulé, B. (2014). Post-crisis analysis of an ineffective tsunami alert: the 2010 earthquake in Maule, Chile. *Disasters*, *38*, 375–397. <https://doi.org/10.1111/disa.12045>
- Strandberg, J., Hobiger, T., & Haas, R. (2016). Improving GNSS-R sea level determination through inverse modeling of SNR data. *Radio Science*, *51*, 1286–1296. <https://doi.org/10.1002/2016RS006057>
- Williams, S. D. P. (2020). *NOCTidefit*. <https://git.noc.ac.uk/noc-tide-gauges/noc-tgqc/-/blob/master/NOCTidefit>
- Yamazaki, Y., & Cheung, K. F. (2011). Shelf resonance and impact of near-field tsunami generated by the 2010 Chile earthquake. *Geophysical Research Letters*, *38*, L12605. <https://doi.org/10.1029/2011GL047508>
- Yamazaki, Y., Cheung, K. F., & Kowalik, Z. (2011). Depth-integrated, non-hydrostatic model with grid nesting for tsunami generation, propagation, and run-up. *International Journal for Numerical Methods in Fluids*, *67*(12), 2081–2107. <https://doi.org/10.1002/flid.2485>
- Yamazaki, Y., Cheung, K. F., & Lay, T. (2018). A self-consistent fault slip model for the 2011 Tohoku earthquake and tsunami. *Journal of Geophysical Research: Solid Earth*, *123*, 1435–1458.
- Yamazaki, Y., Kowalik, Z., & Cheung, K. F. (2009). Depth-integrated, non-hydrostatic model for wave breaking and run-up. *International Journal for Numerical Methods in Fluids*, *61*(5), 473–497. <https://doi.org/10.1002/flid.1952>
- Yoshimoto, M., Watada, S., Fujii, Y., & Satake, K. (2016). Source estimate and tsunami forecast from far-field deep ocean tsunami waveforms—The 27 February 2010  $M_w$  8.8 Maule earthquake. *Geophysical Research Letters*, *43*, 659–665. <https://doi.org/10.1002/2015GL067181>



## **Dynamic Sea Level Variation from GNSS: 2020 Shumagin Earthquake Tsunami Resonance and Hurricane Laura**

**Kristine M. Larson<sup>1</sup>, Thorne Lay<sup>2</sup>, Yoshiki Yamazaki<sup>3</sup>, Kwok Fai Cheung<sup>3</sup>, Lingling Ye<sup>4</sup>, Simon D.P. Williams<sup>5</sup>, and James L. Davis<sup>6</sup>**

<sup>1</sup>Department of Aerospace Engineering Sciences, University of Colorado, Boulder, CO, USA

<sup>2</sup>Department of Earth and Planetary Sciences, University of California, Santa Cruz, CA, USA

<sup>3</sup>Department of Ocean and Resources Engineering, University of Hawaii at Manoa, Honolulu, HI, USA

<sup>4</sup>Guangdong Provincial Key Lab of Geodynamics and Geohazards, School of Earth Sciences and Engineering, Sun Yat-sen University, Guangzhou, China

<sup>5</sup>National Oceanography Centre, Liverpool, United Kingdom

<sup>6</sup>Lamont Doherty Earth Observatory, Columbia University, Palisades, N.Y., USA

### **Contents of this file**

Figures S1 to S4

### **Introduction**

This supporting information is comprised of four figures that supplement the material presented in the main text.

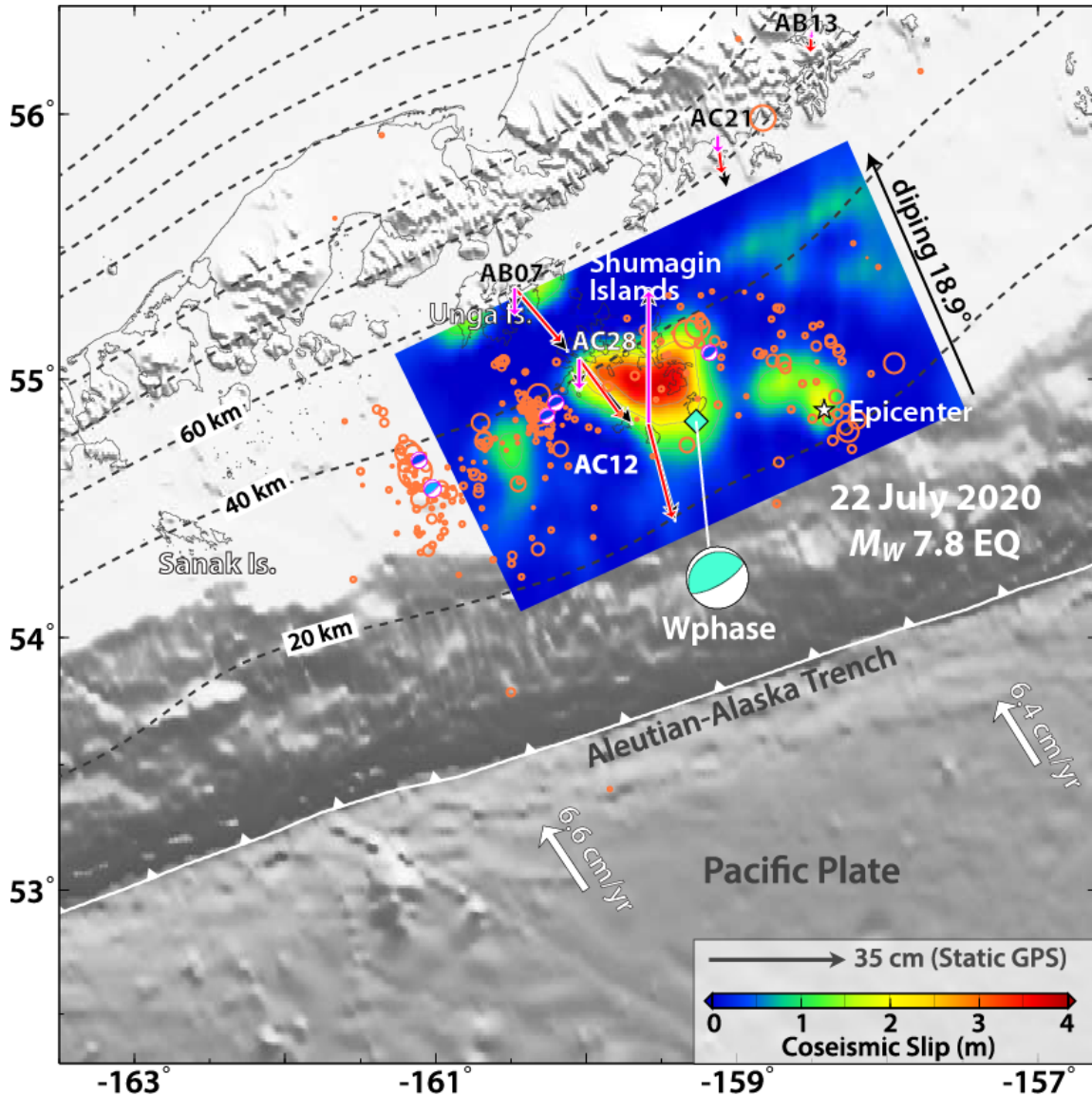


**Figure S1.** Slip distribution for the 22 July 2020 Shumagin Islands  $M_W$  7.8 earthquake obtained from joint inversion of teleseismic  $P$  and  $SH$  waves and regional GNSS-observations (manuscript currently in review, Ye, et al., The 22 July 2020  $M_W$  7.8 Shumagin seismic gap earthquake: partial rupture of a weakly coupled megathrust. *Earth and Planetary Science Letters*). The colored rectangle depicts the extent of the model on the  $18.9^\circ$  dipping plate-boundary megathrust fault. The star indicates the epicenter, with the rupture initiating 23 km below the surface. The GNSS stations are shown with horizontal and vertical displacements indicated by black vectors, and model predictions of vertical (magenta) and horizontal (red) displacement. The focal mechanism (lower hemisphere projection with compressional quadrant in cyan) is from inversion of W-phase observations for a point source, and the cyan diamond indicates the centroid location. The orange circles are locations of aftershocks in the first month after the event from the Alaskan Seismic Network. The white vectors indicate motion of the Pacific Plate relative to a fixed North American plate. The dashed contours indicate the depth of the plate boundary contact from the model SLAB2 (Hayes et al., 2018).

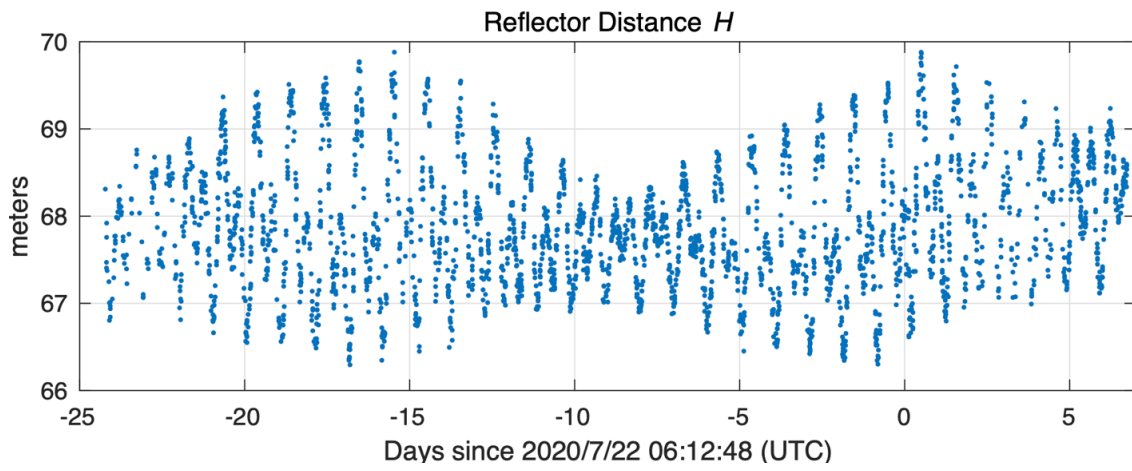


**Figure S2.** GNSS-IR  $H$  estimates for Chernabura, Alaska GNSS site AC12.

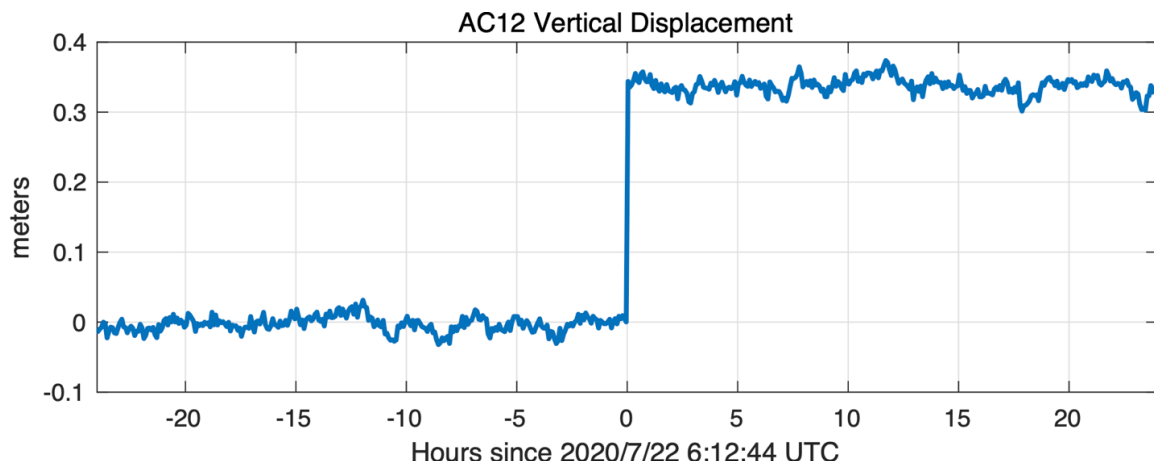


**Figure S3.** AC12 vertical position estimates on the days before and after the Shumagin Islands earthquake (Blewitt et al., 2018). Estimates are shown for a five-minute sample rate.

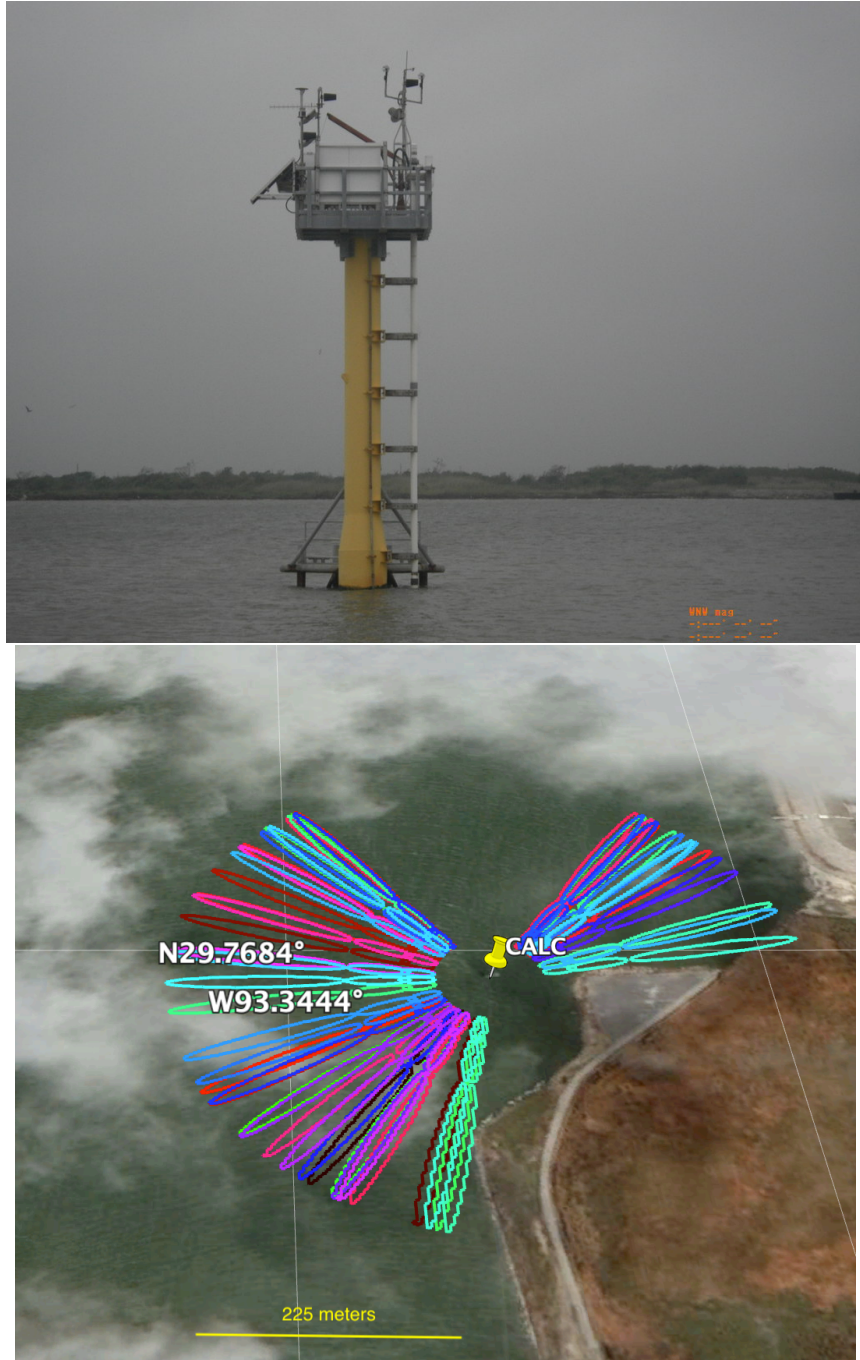


**Figure S4.** GNSS receiver at Calcasieu Pass, Louisiana. Top: GNSS antenna is located on the left side of the sentinel. Bottom: Colored regions show reflection zones used for water level measurements. Photo credit: National Geodetic Survey; Map credit: Google Earth.